Check for updates

THE AMERICAN SOCIETY OF MECHANICAL ENGINEERS
345 E. 47th St., New York, N.Y. 10017

98-GT-173

The Society shall not be responsible for statements or opinions advanced in papers or discussion at meetings of the Society or of its Divisions or Sections, or printed in its publications. Discussion is printed only if the paper is published in an ASME Journal. Authorization to photocopy for internal or personal use is granted to libraries and other users registered with the Copyright Clearance Center (CCC) provided $3/article or $4/page is paid to CCC, 222 Rosewood Dr., Danvers, MA 01923. Requests for special permission or bulk reproduction should be addressed to the ASME Technical Publishing Department.

Copyright © 1998 by ASME All Rights Reserved Printed in U.S.A.

HEAT TRANSFER AND FLOWFIELD MEASUREMENTS IN THE LEADING EDGE REGION OF A STATOR VANE ENDWALL

M. B. Kang, A. Kohli*, and K. A. Thole
Mechanical Engineering Department
University of Wisconsin
Madison, Wisconsin 53706

Abstract

The leading edge region of a first stage stator vane experiences high heat transfer rates especially near the endwall making it very important to get a better understanding of the formation of the leading edge vortex. In order to improve numerical predictions of the complex endwall flow, benchmark quality experimental data are required. To this purpose, this study documents the endwall heat transfer and static pressure coefficient distribution of a modern stator vane for two different exit Reynolds numbers (Re_{ex} = 6 x 10^5 and 1.2 x 10^6). In addition, laser Doppler velocimeter measurements of all three components of the mean and fluctuating velocities are presented for the stagnation plane in the leading edge region. Results indicate that the endwall heat transfer, pressure distribution and flowfield characteristics change with Reynolds number. The endwall pressure distributions show that lower pressure coefficients occur at the higher Reynolds number due to secondary flows. The stronger secondary flows cause enhanced heat transfer near the trailing edge of the vane at the higher Reynolds number. On the other hand the mean velocity, turbulent kinetic energy and vorticity results indicate that leading edge vortex is stronger and more turbulent at the lower Reynolds number. The Reynolds number also has an effect on the location of the separation point which moves closer to the stator vane at the lower Reynolds number.

Introduction

Increasing exiting combustor temperatures for future gas turbine designs lends itself to high heat load demands on downstream turbine vanes. One of the regions having the highest heat transfer is where the leading edge of the vane meets the endwall. As the endwall boundary layer approaches the stagnation location of the protruding turbine vane, it experiences an increase in pressure causing a stronger deceleration for the higher speed fluid than the lower speed fluid in the boundary layer. As a result of these differences in the deceleration, a transverse pressure gradient occurs along the vane causing the higher speed fluid to turn toward the endwall plate. Subsequently, the formation of a horseshoe vortex occurs just upstream of the turbine vane. One of the legs of the horseshoe vortex wraps around the pressure side of the vane and the other around the suction side of the vane.

There have been quite a few studies documenting endwall characteristics for rotors, but fewer stator vane studies, which typically have less of a turning angle and higher flow accelerations than rotors where both effects are believed to influence the secondary flows. Based on previously reported studies, there is still a need for a better understanding of the endwall flow particularly in the leading edge region where the leading edge horseshoe vortex is formed and its relationship with secondary flows in the passage. Before computational efforts can expect to simulate the complex flowfield in the vane passage, it is imperative that the leading edge horseshoe vortex can be correctly predicted. This study involves quantifying the surface heat transfer as well as the horseshoe vortex that occurs in the leading edge endwall region of a modern turbine vane geometry. Highly-resolved surface heat transfer measurements, made through the use of an infra-red camera, will be reported for two different Reynolds numbers. In addition to surface heat transfer measurements, flow field measurements of the leading edge vortex, and a comparison of measured and CFD predicted endwall static pressure will be discussed.

Past Studies

As mentioned earlier, many of the endwall investigations presented in the open literature have used airfoil geometries that have high turning angles being more representative of rotor geometries. Sieverding (1985) presents a summary of endwall flowfield models for rotor passages including one of the first models as presented by Langston, et al. (1977). All of these studies imply the formation of the horseshoe vortex at the leading edge-endwall intersection with a pressure-side leg and suction-side leg.

Since the blade curvature is an important effect in setting up the secondary flows, it is difficult applying these same results to a stator vane having a smaller turning angle. This fact is illustrated by Bailey (1980) in which he compared vane flowfield measurements by Marchal and

* Present address is Pratt & Whitney, 400 Main Street, MS 169-02, East Hartford, CT 06108

Presented at the International Gas Turbine & Aeroengine Congress & Exhibition
Stockholm, Sweden — June 2–June 5, 1998
This paper has been accepted for publication in the Transactions of the ASME
Discussion of it will be accepted at ASME Headquarters until September 30, 1998

Downloaded from http://asmedigitalcollection.asme.org/GT/proceedings-pdf/GT1998/78651/V004T09A035/2411331/v004t09a035-98-gt-173.pdf by guest on 20 August 2022

Sieverding (1977) to rotor flowfield measurements by Langston, et al. (1977). This comparison was made near the exits of the vane and rotor passages which showed that the extent of the passage vortex was much greater for the vane than for the rotor. In addition, while the passage vortex was centered halfway between the suction and pressure surface for the vane, it was located nearer to the suction surface in the rotor. Bailey himself presented flowfield measurements for the endwall of a turbine vane in which his results concurred with Marchal and Sierverding's (1977), but was complicated by the fact that his test facility did not simulate the leading edge vortex.

Graziani, et al.(1980) who used the same rotor geometry as Langston, et al. (1977) compared differences between a boundary layer that was thick (15% of the span) and thin (2% of the span) at the same inlet Reynolds numbers. One could, however, consider these two cases to be a high Re_θ for the thick boundary layer and a low Re_θ for the thin boundary layer where θ is the momentum thickness. This is in contrast to the results that will be discussed for our paper (in Table 2) whereby the higher Re_θ occurs for the thinner boundary layer. This difference in the relations between thick and thin boundary layers and momentum thicknesses occurs because nf how the experiments were conducted. While we maintained the same upstream endwall plate length and only changed the freestream velocity to vary the Reynolds number, Graziani, et al. (1980) maintained the same inlet velocity and shortened their upstream endwall length.

Graziani, et al. (1980) showed for their surface streakline visualization at the low Re_θ case (thin boundary layer) there was less cross-over of the ink traces toward the suction side of the airfoil. Although the traces on the blade indicated that for both Re_θ cases there was a movement of the traces towards the midspan of the blade, the high Re_θ case had traces that crawled further toward the midspan of the blade as compared with the low Re_θ case. As stated by Graziani, et al. (1980) both of these results indicate that for the higher Re_θ the passage vortex occupies more of the passage in this region which would then subject the suction side of the adjacent airfoil to be affected greater by secondary flow effects. The Stanton numbers are also consistent with this in that the contours for the high Re_θ case was more affected by the path of the vortex. Their endwall static pressure measurements, however, indicate lower pressure coefficients for the low Re_θ case whereby a lower pressure coefficient would be more consistent with a lift-off of the passage vortex. This can be explained, however, by the fact that Graziani, et al. (1980) maintained the same inlet velocity and changed the boundary layer by changing the approach plate length. In this case, the actual mass flowrate going through the passage would be more for the thinner boundary layer case and one would expect a larger decrease in the static pressure.

Although the previous data indicates a stronger passage vortex at higher Reynolds number, the data of Graziani,et al. (1980) was presented for a rotor. Boyle and Russell (1990) performed experiments for a large Reynolds number range for a stator vane geometry. At low Reynolds numbers, they found that Stanton number contours closely followed the inviscid streamlines from the pressure side to the suction side of the airfoil while at higher Reynolds numbers the surface heat transfer correlates closely with the freestream velocity and thereby looks more similar to the static pressure contours.

Because the leading edge-endwall location typically has high heat transfer, particular attenuon has been paid to that region. On the endwall, one of the regions having the highest heat transfer coefficient is near where the airfoil leading edge meets the endwall. In relating information from the flow visualization to the heat transfer data, Gaugler and Russell (1984) combined two studies, their own and that of York, et al. (1984), for a large scale turbine vane in which they found the peak Stanton number to coincide with the region having the most intense vortex action. They also found near the suction surface a secondary peak in Stanton number, which coincided with the region where the endwall separation line contacts the suction surface at the point where the flow started to climb the suction surface.

Comparisons made by Boyle and Russell (1990) for endwall leading edge heat transfer for various Reynolds numbers and approach plate lengths indicated that heat transfer augmentations was higher at lower Reynolds numbers. Based on their heat transfer measurements for the thick and thin boundary layer cases, Graziani, et al. (1980) postulated that the boundary layer separation due to the horseshoe vortex for the thinner inlet boundary layer was closer to the airfoil than for the thicker inlet boundary layer. In comparing two independent studies where the momentum thickness was the same, including the studies of Goldstein and Spores (1988) and Graziani, et al. (1980), the Stanton number values and trends in the leading edge region were similar even though the Reynolds number was four times greater for Graziani et al. These results would indicate that for a rotor there is only a weak dependence on Reynolds number.

Nomenclature

C	=	true chord of stator vane
C_p	=	pressure coefficient, $C_p = (p - p_{in}) / 1/2\rho U^2_{in}$
D	=	diameter of vane leading edge, 2R
H	=	shape factor, δ^* / θ
k	=	turbulent kinetic energy, $k = 1/2 (u^2_{rms} + v^2_{rms} + w^2_{rms})$
p	=	static pressure
R	=	radius of vane leading edge
Re_{cx}	=	Reynolds number defined as $Re_{cx} = C U_{ex} / \nu$
Re_D	=	Reynolds number defined as $Re_D = 2 R U_{in} / \nu$
Re_θ	=	Reynolds number defined as $Re_\theta = U_{in} \theta / \nu$
s	=	distance along streamline
S	=	half-span height of stator vane
St	=	Stanton number defined as $St = h / \rho Cp U_{in}$
U, u	=	streamwise mean and fluctuating velocities
U^+	=	mean velocity in wall coordinates, $U^+ = U / \sqrt{\tau_w / \rho}$
U_{in}	=	averaged inlet velocity over two vane pitches
V, v	=	pitchwise mean and fluctuating velocities
W, w	=	spanwise mean and fluctuating velocities
x	=	streamwise distance from stagnation point
y	=	pitchwise distance from stagnation point
z	=	spanwise distance measured from endwall surface
z^+	=	spanwise distance in inner coordinates, $z^+ = z \sqrt{\tau_w / \rho} / \nu$

Greek

δ_{99}	=	boundary layer thickness
δ^*	=	displacement thickness
θ	=	momentum thickness
ε	=	dissipation
ρ	=	density
ν	=	viscosity
ω_y	=	vorticity in the pitchwise direction, $\omega_y = \frac{\partial U}{\partial z} - \frac{\partial W}{\partial x}$
τ_w	=	wall shear stress

Subscripts

avg	=	average
in	=	inlet
ex	=	exit
rms	=	root mean square

Downloaded from http://asmedigitalcollection.asme.org/GT/proceedings-pdf/GT1998/78651/V004T09A035/2411331/v004t09a035-98-gt-173.pdf by guest on 20 August 2022

The only study in which the leading edge vortex has been measured is that presented by Pierce and Harsh (1988) who used a streamlined cylinder normal to a flat plate where the $Re_D = 1.7x10^5$, based on the inlet velocity, and having a boundary layer thickness-to-cylinder diameter ratio of $\delta_{99}/D = 0.63$. These results indicated a single vortex where the center of that vortex is located approximately 0.8D upstream of the cylinder. Heat transfer data reported by Goldstein and Spores (1988), however, had two peaks that near the leading edge indicated the presence of a corner vortex, causing an intense spike in the mass transfer coefficients, and the presence of the horseshoe vortex, causing a slight rise in the mass transfer coefficients. The flowfield data of Pierce and Harsh (1988) indicate only a single vortex but, as pointed out by Pierce and Harsh, this may be due to the resolution of the grid. In addition, because the data was acquired with a pitot probe, there was no information regarding the turbulence field associated with the horseshoe vortex region itself.

Based on past studies there is a clear need to further investigate the heat transfer characteristics of the endwall of a commercial stator vane. Although there has been a link between flowfield visualization and surface heat transfer measurements, a link between measured flowfields and measured heat transfer is still needed. In particular, it is clear that the formation of the leading edge horseshoe vortex still needs to be understood and that there is still a need to provide benchmark data for computational studies.

Experimental Design

A modern stator vane, scaled up by a factor of nine, was placed in a large-scale wind tunnel for this study. The construction and the development of the scaled-up stator turbine vane and the test section has been documented by Bangert, et al. (1997). Some modifications were made to the facility described in the above mentioned study and these will be addressed in this paper. The wind tunnel used in this study is a large recirculating wind tunnel which contains a square test section and a corner test section. Figure 1 shows the corner test section which contains a scaled-up central turbine vane and two leading edges, representing the two adjacent vanes, which are attached to flexible side walls. The adjacent leading edges were included to insure that the passage vortex was correctly simulated in these experiments. The side wall boundary layers were removed by an adjustable bleed on one side and a suction box on the other to insure that the stagnation point was positioned correctly on the outer leading edges. This allowed for a periodic flow in both passages around the central airfoil. A heat flux plate was placed on the bottom endwall while various lids were placed on the top endwall depending upon the type of measurements that were needed, as will be described later. The flow was prevented from going from the pressure to the suction sides under the vane by applying a sealant at the base of the vane. A description of the turbine vane itself is given by Table 1.

The major modification to the test section of Bangert, et.al. for this study was the use of both the top and bottom endwalls. The heat transfer measurements were made on the bottom endwall while the static pressure and flowfield measurements were made on the top endwall. For this reason it was important to match the inlet boundary layer for the top and bottom endwalls. Boundary layer growth was controlled using splitter plates of length 2.45 m (or 4.1 vane chords) installed upstream of the test section inside the diffuser. The flow approaching the stator vane test section is decelerated by the diffuser only in the lateral direction while the distance across the span of the turbine vane is held fixed from the start of the splitter plates to the turbine vane. The splitter plates allow flow from the top and the bottom of the diffuser to be diverted which is then redirected into the wind tunnel downstream of the stator vane test section. This diverted airflow was controlled using valves to insure that

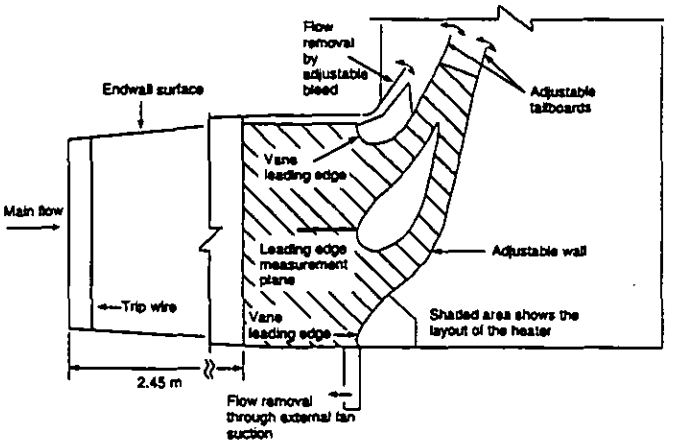

Fig. 1 View of the corner turbine vane test section.

the same boundary layer conditions are met on both the top and bottom walls. The flow was tripped at the start of the splitter plates to obtain fully turbulent boundary layers at the inlet to the stator vane test section. The endwall heat transfer and flowfield was investigated for two Reynolds numbers of $Re_{ex} = 6 \times 10^5$ and 1.2×10^6.

Table 1. Geometrical and Flow Conditions for Stator Vane

Actual chord length	6.60 cm
Scaling factor	9
Scaled-up chord length	59.4 cm
Pitch/chord	0.77
Span/chord	0.93
Exit Reynolds number	$1.2x10^6$
Flow inlet angle	0°
Flow exit angle	78°
Approach length/chord	4.1

Inlet Boundary Layer and Streakline Visualization

Inlet boundary layer measurements using the laser Doppler velocimeter were done one chord upstream of the stator vane test section on the top and bottom endwalls. These are shown in Figure 2a for both the high and low Reynolds number cases and the corresponding boundary layer parameters are listed in Table 2. Note that the incident turbulence level upstream of the vane was 0.9%. The results show that there is very good agreement between the boundary layers on the top and bottom endwalls. The ratio of boundary layer thickness to half-span height is $\delta_{99}/S = 0.21$ and $\delta_{99}/S = 0.18$ for the low and high Reynolds number cases respectively. The shape factors for these boundary layers are higher than those predicted by a zero-pressure gradient correlation, but this is expected as the boundary layers experience an adverse pressure gradient in the diffuser section of the wind tunnel. The decrease in boundary layer thickness as the Reynolds number is increased between the two cases can be predicted based on a flat plate turbulent boundary layer correlation to be an decrease of 87%, which is consistent with the data presented in Table 2. Note that for these endwall studies the Reynolds number, based on the incident velocity and chord length are different by a factor of two, but the boundary layer thickness itself is only a factor of 15% different.

Figure 2b shows the surface streakline patterns on the endwall for the high Reynolds number case, $Re_{ex} = 1.2x10^6$. These streaklines were obtained by painting a mixture of black paint, kerosene, and machine oil on shelf paper that was placed on the endwall. After the mixture was painted on the endwall, the wind tunnel was turned on and after about two hours a steady state pattern was achieved. This pattern is very similar to those

Downloaded from http://asmedigitalcollection.asme.org/GT/proceedings-pdf/GT1998/78651/V004T09A035/2411331/v004t09a035-98-gt-173.pdf by guest on 20 August 2022

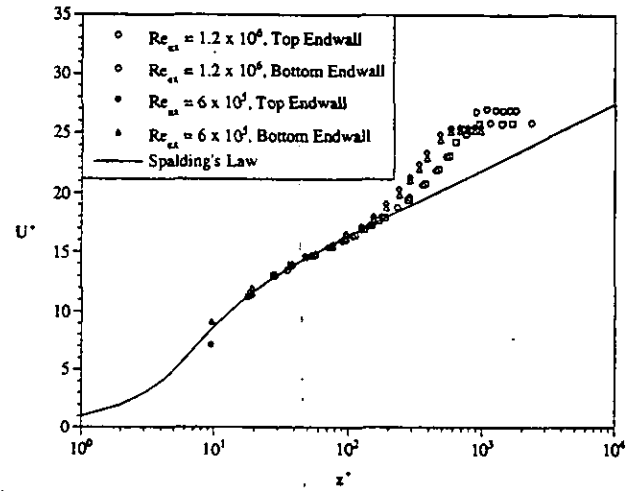

Fig. 2a Inlet boundary layers measured one chord upstream for two Reynolds numbers on top and bottom endwalls.

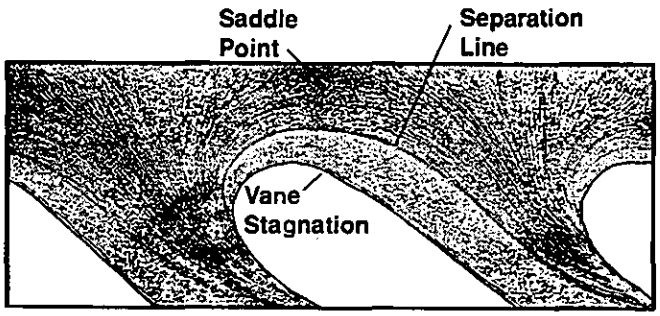

Fig. 2b Endwall streakline visualization for Re_{ex} = 1.2 x 10⁶.

Table 2. Inlet Boundary Layer Characteristics

	Re_{ex} = 6 x 10⁵		Re_{ex} = 1.2 x 10⁶	
	Top	Bottom	Top	Bottom
δ_{99} (cm)	5.8	5.8	5.0	4.8
δ^* (cm)	1.20	1.21	1.06	0.92
θ (mm)	7.8	7.9	7.1	6.2
H	1.55	1.52	1.50	1.48
Re_θ	1870	1900	3340	2960
U (m/s)	3.73	3.70	7.33	7.45

previously reported in the literature. A saddle point is clearly seen upstream of the stagnation location of the vane. The separation line is also clearly seen starting from the suction side of the vane and intersecting with the adjacent vane. This separation line occurs at a streamwise distance upstream of the stagnation location that is x/R = -0.76 for Re_{ex} = 1.2x10⁶ and slightly closer to the vane at x/R = -0.69 for Re_{ex} = 5x10⁵ (not shown here). This location of the separation line occurs at a position consistent with where the flowfield measurements indicate a reverse flow direction (as will be discussed later in the text for Figures 9a and 9b).

Static Pressure Measurements

As mentioned earlier, a different top endwall was designed and installed for the static pressure measurements. Static pressure taps were made using brass tubes with an inside diameter of 0.79 mm. These taps were 9.5 mm long which resulted in a length-to-diameter ratio of 12. The measuring end of the tube was chamfered using a 82° countersink. These parameters were chosen to give the most accurate static pressure measurements based on

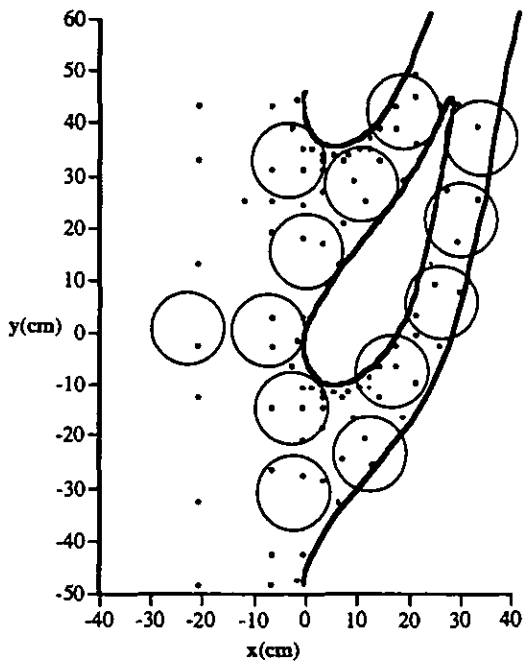

Fig. 3 Schematic of pressure tap locations and viewing ports for the infra-red camera measurements.

the recommendations of Mattingly (1996). The pressure taps were connected using flexible vinyl hose to two scanivalves (Scanivalve W0602/1P-24T Fluid Switch Wafer) which were connected to two differential pressure transducers (Omega PX 653) with pressure ranges of 0 - 0.5 and 0 - 2.0 inches of water. Voltage data from the pressure transducers were acquired using a National Instruments A/D board (AT-MIO-16E-2) and controlled using National Instrument's LabVIEW, software.

A total of 93 pressure taps were installed for the endwall static pressure measurements and are shown in Figure 3. The locations of these taps were determined using CFD predictions of the endwall pressure coefficient, Cp, distribution. The CFD solution was sampled at selected locations and the static pressure contours were plotted using just those locations. Pressure locations were added till the pressure gradients were resolved sufficiently and the contours looked smooth. This resulted in a highly non-uniform distribution of the pressure taps as can be seen clearly in Figure 3. For these pressure measurements 5,000 samples were acquired at every location at a sampling frequency of 1 kHz. The uncertainty in the pressure measurements from repeatability and run-to-run variations was estimated to be ± 0.05 Cp. The total uncertainty in the pressure coefficient results including a 1% uncertainty in the inlet velocity was estimated to be ± 0.25 Cp.

Heat Transfer Measurements

Heat transfer measurements were made on the bottom endwall of the test section. A constant heat flux plate, manufactured by Electrofilm Manufacturing, was designed to surround the styrofoam stator vane. The heater itself consists of a 50 μm thick copper layer on top of a 75 μm thick kapton layer within which 25 μm thick inconel heating elements were embedded in a serpentine pattern. The heater was then attached to the bottom endwall using double-sided tape. The total area of the heat flux plate was 0.549 m². Using a variac, the heat flux was varied between 400 and 800 W/m² for the two Reynolds numbers investigated in this study. The bottom endwall was made of 1.9 cm thick plywood and insulated below by a 2.54 cm thick R-5 extruded styrofoam. Lateral conduction in the copper layer was estimated to be less than 1% when considering the spot size over which the infra-red camera averages the

Downloaded from http://asmedigitalcollection.asme.org/GT/proceedings-pdf/GT1998/78651/V004T09A035/2411331/v004t09a035-98-gt-173.pdf by guest on 20 August 2022

surface temperatures. On the top surface of the heater, where measurements were made, four E-type ribbon thermocouples were placed using electrically insulating epoxy for calibration of the infra-red camera. The top surface of the heater plate and the thermocouples were painted black. The freestream temperature for these cases was nominally 21°C.

An infra-red camera (Inframetrics Model 760) was used to collect the surface temperature information from the constant heat flux plate on the bottom endwall. The camera was calibrated insitu using a thermocouple placed on the heater surface. The correct plate emissivity and background temperature was determined over the required measurement temperature range thereby giving a linear relationship between the thermocouple reading and infra-red camera measurement. For these measurements, the top endwall was replaced with one which had 13 viewing ports that were 11.43 cm in diameter, whereby either a lexan insert or a crystal flouride window were placed. These viewing ports are shown in Figure 3. The crystal flouride window has characteristics of being 98% transmissive over the 8 to 12 μm wavelength range, which is the operating range of the camera. The crystal fluoride window was moved to each of the 13 viewing ports and an image was recorded. Each image was an average of 16 images and, based on an uncertainty analysis, it was determined that five of these 16-averaged images were enough to get a good average of the endwall temperatures. Some of the images from the 13 viewing ports spatially overlapped and, in those cases, the temperatures were averaged to get a final temperature for those endwall positions.

The camera was operated at its maximum viewing area of 21.5 cm x 16 cm which it digitized onto 255 x 206 pixels. The spot size over which the infrared camera performed a spatial integration was 0.37 cm or, for comparison with the dimensions in terms of vane chords, was 0.0062 C. Small positioning crosses were placed on the endwall to identify where each of the pictures were taken. Temperature data from the camera were processed using ThermoMonitor Lite software, manufactured by Thermoteknix Systems Ltd, which gave the temperature data at each pixel. For each picture, the positioning crosses were used to scale and transform data at each pixel to its corresponding position on the endwall. A processing routine was written in-house to assemble all of the pictures into one complete picture of the endwall temperature distribution.

The input heat flux was corrected for radiation losses, which amounted to between 4 - 23 % of the input power, and conduction losses, which amounted to 1.7 -3.5 % of the input power. No correction was necessary regarding heat losses from conduction to the turbine vane itself because the vane was constructed using styrofoam (Bangert, et al., 1997). Using the measured temperatures and the remaining convective heat flux, the heat transfer coefficients were computed and put in terms of a Stanton number based on the inlet velocity of 3.2 m/s for $Re_{ct} = 6x10^5$ and 6.4 m/s for $Re_{ct} = 1.2x10^6$. The uncertainty in the Stanton number for a temperature difference of 5°C is ±3.5% and 3% for the low and high Reynolds number cases, respectively. This uncertainty was dictated by the uncertainty in measuring the temperature and therefore is highest at the lowest temperature difference (5°C).

Flowfield Measurements

All three components of velocity were measured using a two-component LDV on the stagnation plane to quantify the leading edge vortex at the two different Reynolds numbers. Since this is a plane of symmetry, V, the pitchwise velocity component was nominally zero. This component, however, was measured such that a total turbulent kinetic energy approaching the vane could be computed. The two-component backscatter fiberoptic LDV system used in this study consists of a 5 W Coherent laser used in conjunction with a TSI model 9201 Colorburst beam separator. Velocity data were processed using TSI model IFA 755 Digital Burst Correlator controlled using TSI's FIND software. Two different focusing lenses (350 mm and 750 mm) were used for these measurements. The 350 mm focusing lens was used to make measurements of the streamwise and pitchwise components through the top endwall. The spanwise component was measured from the side using the 750 mm focusing lens.

The velocity measurement plane was over a region 7.6 cm x 7.6 cm in area. Velocity profiles were measured at 15 streamwise locations with 14 points each in the spanwise direction for a total of 210 measurement locations. Distance between the profiles in the streamwise direction was kept fixed at 0.0085C while the measurement locations in the spanwise direction were concentrated near the endwall to discern the leading edge vortex. At each measurement location for each component of velocity 10,000 data points were used to compute the mean and turbulence quantities. The data were corrected for velocity bias effects by applying the residence time weighting. Uncertainties in the mean velocity is estimated to be ±1% while the precision uncertainties, based on a 95% confidence interval, for the rms of the velocity fluctuations were 3.0% in the highly turbulent regions.

Results

Results for the two Reynolds numbers investigated in this study are presented first in terms of pressure coefficient and Stanton number contours on the endwall. Next, the flowfield results on the stagnation plane are presented in terms of mean velocity vectors and contours of the turbulent kinetic energy and vorticity.

Endwall Static Pressure

Before the endwall static pressure results are discussed it is useful to study the pressure distribution along the mid-span of the vane. This allows us to separate the effect of secondary flows from the bulk motion. Figure 4a gives the static pressure measurements, in terms of the pressure coefficient for the low and high Reynolds number cases at a spanwise location that is 40% up from the bottom endwall. The results have been presented as normalized distance along the vane surface, with the pressure side on the left and the suction side on the right. The strong acceleration on the suction side of the vane is clear from the rapidly decreasing value of Cp through s/C = 0.3. The flow continues to accelerate at a smaller rate until s/C = 0.5 after which the velocity stays relatively constant with Cp ~ -27. Note that there are slightly lower values of Cp for the high Reynolds number case. The flow slows down slightly beyond s/C = 1 near the trailing edge of the vane. Unlike the suction side of the vane, flow on the pressure side of the vane accelerates monotonically.

The pressure coefficient results for $Re_{ct} = 6x10^5$ and $1.2x10^6$ on the endwall are shown in Figures 4b and 4c. Note that the measurements indicate good periodicity between the two passages surrounding the airfoil. On the endwall, the largest difference between the two Reynolds numbers is a larger low pressure region on the endwall for the high Reynolds number case where there is a contour level of Cp = -27.5 as compared with the low Reynolds number case where there is just a small region having a minimum value of Cp = -25. This is due to the secondary flow which is much stronger at the high Reynolds number case. As the secondary flow separates from the endwall, one would expect a low pressure region to occur resulting in a lower Cp value. This was also evident beyond s/C = 0.5, on the suction side of the vane at the midspan as discussed already.

Surface oil visualization studies along the vane span and in the passage endwall were done for this turbine vane at both the high and low Reynolds numbers. There were two primary differences between the low and high Reynolds number cases. First, the boundary layer separation

Downloaded from http://asmedigitalcollection.asme.org/GT/proceedings-pdf/GT1998/78651/V004T09A035/2411331/v004t09a035-98-gt-173.pdf by guest on 20 August 2022

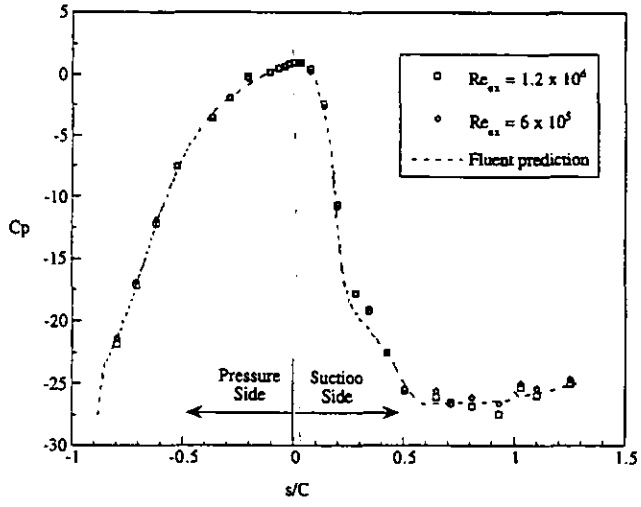

Fig. 4a Static pressure distribution at the vane midspan.

point moved further upstream from the stagnation point for the higher Reynolds number case, as discussed earlier. Second and probably the most interesting result was the fact that at the high Reynolds number, oil from the endwall was carried up onto the suction side of the vane surface, starting at approximately s/C = 0.5. The location at which the paint/oil mixture was found on the vane occurs where the decrease in the static pressure levels off. The oil/paint mixture propagated to a spanwise position of z/S = 0.14. In contrast, there was no oil/paint mixture that propagated onto the vane for the low Reynolds number case. These results are consistent with the fact that there was a larger low pressure region on the endwall for the higher Reynolds number case.

In order to benchmark the above experimental results CFD predictions of the endwall pressure distribution were done using FLUENT/UNS for $Re_{ex} = 1x10^6$. As mentioned earlier, these CFD predictions were also used to design the static pressure endwall with the pressure taps. As these simulations are not the focus of this study, only a brief description is given here. The computational domain modeled just one passage with the suction side and pressure side of the vane as boundary walls. This along with periodic boundaries at the stagnation plane and the trailing edge made the domain periodic in the pitchwise direction. An inlet boundary layer thickness of 5 cm was used for these simulations and inlet velocity, k and ε profiles were generated using the boundary layer code TEXSTAN (Crawford, 1986). An outflow boundary condition was imposed after the trailing edge of the domain and a symmetry boundary condition was applied at the mid-span height. Some of these boundary conditions are identified in Figure 4d which shows the pressure coefficient contours on the endwall. The comparison for the high Reynolds number show that there is a good agreement between the predicted and measured Cp values. The location and peak value of Cp, agree quite well. The contours do not agree near the trailing edge of the vane because the flexible wall was not simulated in order to make the domain periodic. This was necessary to limit the number of cells which was 360,000 for these simulations. These CFD calculations served as a good benchmark for our measurements.

Endwall Heat Transfer

The heat transfer results in terms of Stanton numbers based on inlet velocity for the two Reynolds numbers are given in Figures 5a and 5b. In the region upstream of the vanes, the Stanton numbers are higher for the lower Reynolds number, which can be expected from a turbulent boundary layer prediction. In both cases, there is a high heat transfer

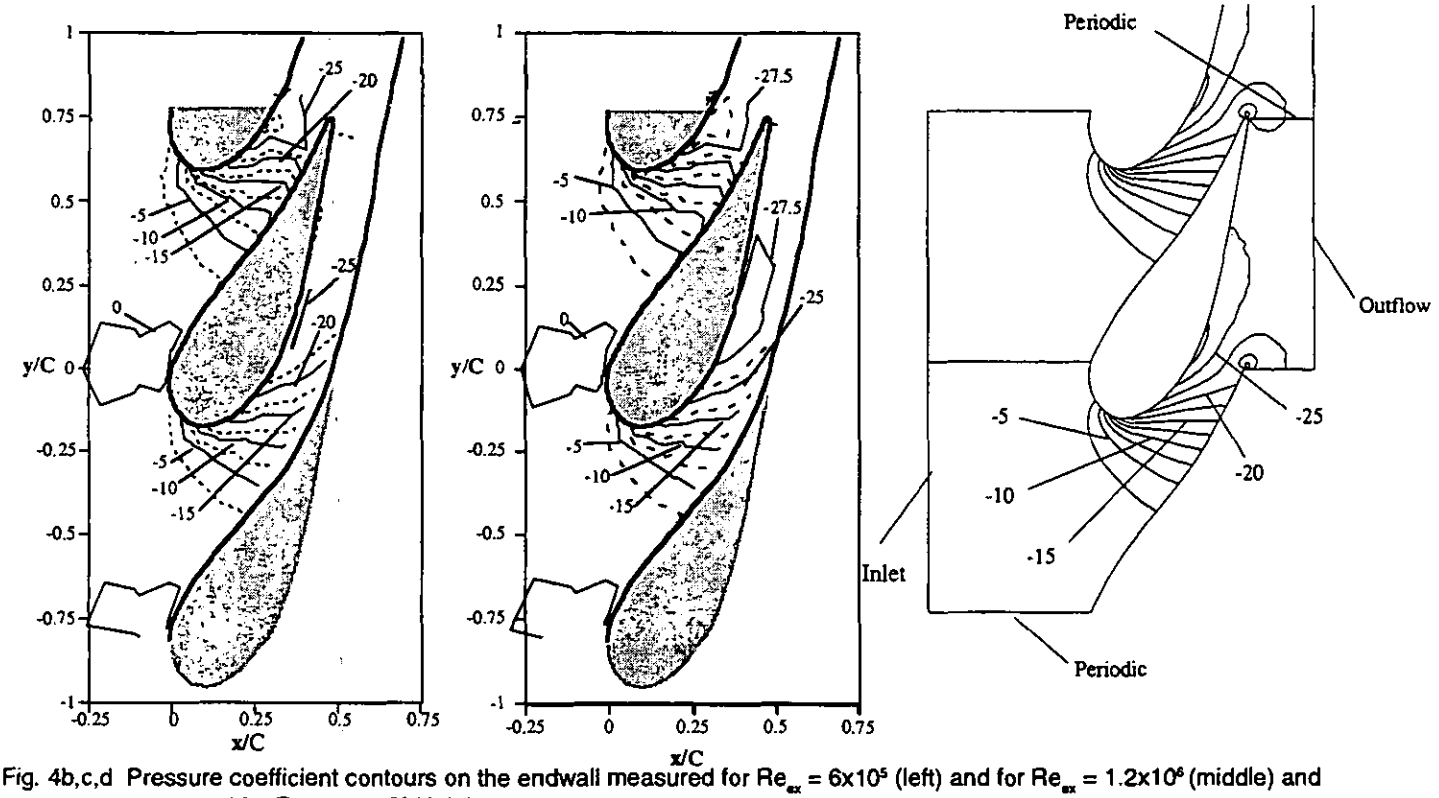

Fig. 4b,c,d Pressure coefficient contours on the endwall measured for $Re_{ex} = 6x10^5$ (left) and for $Re_{ex} = 1.2x10^6$ (middle) and computed for $Re_{ex} = 1x10^6$ (right).

Downloaded from http://asmedigitalcollection.asme.org/GT/proceedings-pdf/GT1998/78651/V004T09A035/2411331/v004t09a035-98-gt-173.pdf by guest on 20 August 2022

region that occurs between the stagnation point and the reattachment of the flow on the suction side of the airfoil. This is the area which experiences very high acceleration as described earlier. As the flow moves through the passage, it is apparent that the location of the peak Stanton numbers are being swept from the outer pressure surface towards the suction side of the central vane. But in the case of the high Reynolds number, the peak local Stanton number occurs at the suction surface-endwall intersection whereas for the low Reynolds number the peak occurred slightly further into the passage and away from the suction surface of the vane. This is consistent with the fact that at the high Reynolds number there is a higher transverse pressure gradient across the passage causing a stronger secondary flow.

The heat transfer distribution near the trailing edge of the central vane is also affected by the flexible tailboard which simulates the pressure side of the adjacent vane because this wall extends beyond where the trailing edge of an adjacent vane would end. Since the goal of this facility was to match engine Reynolds numbers and allow detailed boundary layer measurements on the central vane, the facility was designed to have the smallest number of vanes in order to scale up as much as possible. The flow in the front part of the vane passage is not affected by the tailboard and this can be seen clearly from the good periodicity of the Stanton number and pressure coefficient contours between the two vane passages. Before more flowfield measurements are made inside the vane passage, the effect of the tailboard on the central vane will be quantified using CFD simulations.

Figure 6 shows the pitchwise-averaged Stanton numbers for the two Reynolds number cases. As expected there is a higher average at the lower Reynolds number. Using flat plate turbulent boundary layer correlations, one would predict a 15% increase in the Stanton number based on the change in Reynolds number. These results, however, indicate a larger 25% increase for the lower Reynolds number case. This may be due to an unheated starting length effect which would give slightly larger differences for the two Reynolds number cases. Both the low and high Reynolds number cases, however, show the same trend with just a shift until x/C = 0.35 whereby there is a strong increase for the high Reynolds number case. One plausible explanation for the strong increase is because this is approximately the location where the flow separated off of the endwall, which would be caused by the passage vortex. This location is consistent with the location at which the oil/kerosene mixture was being brought up onto the base of the turbine vane.

Figures 7a and 7b investigate the endwall upstream stagnation region of the vane. Figure 7a shows the Stanton numbers along a line parallel with the flow direction directly in front of the stagnation position. This line corresponds to the surface that is affected by the flowfield plane that was measured upstream of the stagnation, which will be discussed in the next section. Figure 7b indicate that for both cases, the Stanton number starts to increase dramatically upstream of the stagnation between x/R = -1.6 and -1.7 (equivalent to $\Delta x/R = 1.6$ in Figure 7a). As will be shown in the flowfield measurements, this location corresponds to a position upstream of the boundary layer separation point.

Figure 7b gives the augmentation of the heat transfer caused by the leading edge of the turbine vane for the two different Reynolds numbers as compared with those results presented by Boyle and Russell (1990), Hinckel and Nagamatsu (1986) and Ireland and Jones (1986). This augmentation is calculated using the Stanton numbers approaching the stagnation position of the vane divided by the Stanton numbers on the midpitch line. Our data indicate that there is no effect of the Reynolds number on the augmentation. Only very close to the stagnation location is there a large discrepancy between our data and that of Ireland and Jones (1986) who used a cylinder as opposed to an airfoil. Although there is some scatter in the data, the agreement further away from the stagnation position is fairly good. Data from Goldstein and Spores(1988) indicated two peaks for their mass transfer Stanton numbers approaching their rotor blade leading edge. They attributed the peak further away from the blade to the leading edge horseshoe vortex, which is similar to the peak shown in Figure 7b, and the peak closest to the blade stagnation to a corner vortex. Our flowfield measurements, which are discussed in the next section, did not show a corner vortex in our measurement plane

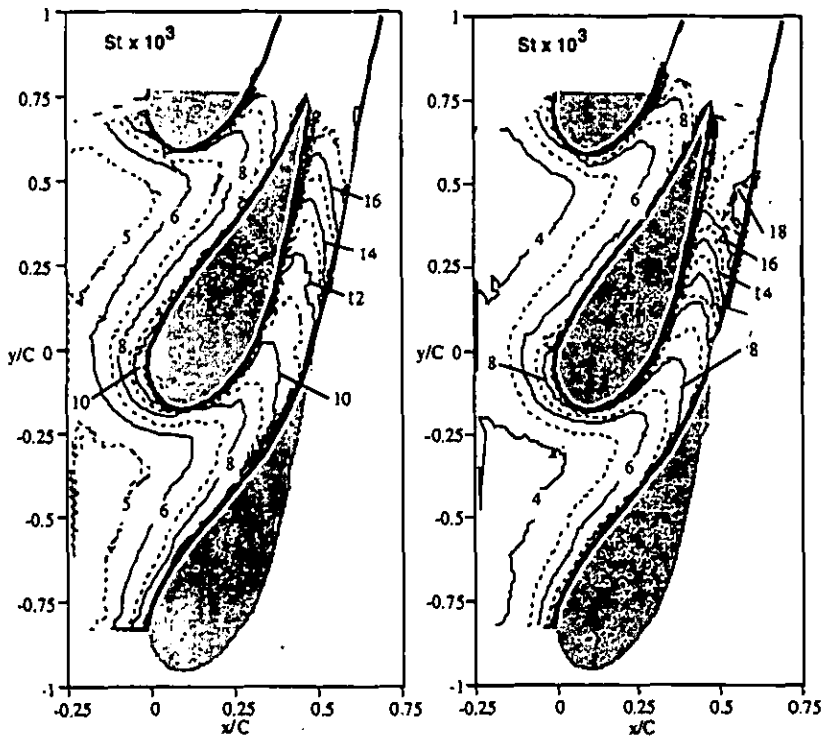

Fig. 5a, b Stanton contours for Re_{ex} = 6x10^6 (left) and 1.2x10^6(right).

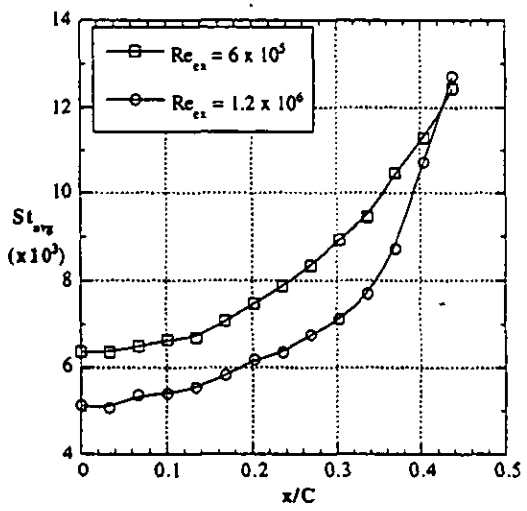

Fig. 6 Pitchwise averaged Stanton numbers in the passage.

Downloaded from http://asmedigitalcollection.asme.org/GT/proceedings-pdf/GT1998/78651/V004T09A035/2411331/v004t09a035-98-gt-173.pdf by guest on 20 August 2022

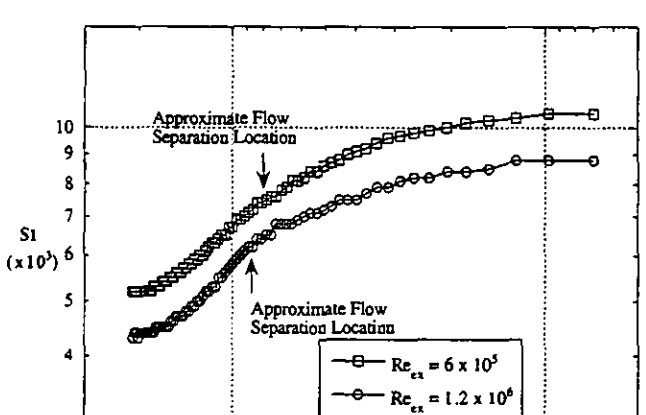

Fig. 7a Stanton numbers upstream of turbine vane stagnation point.

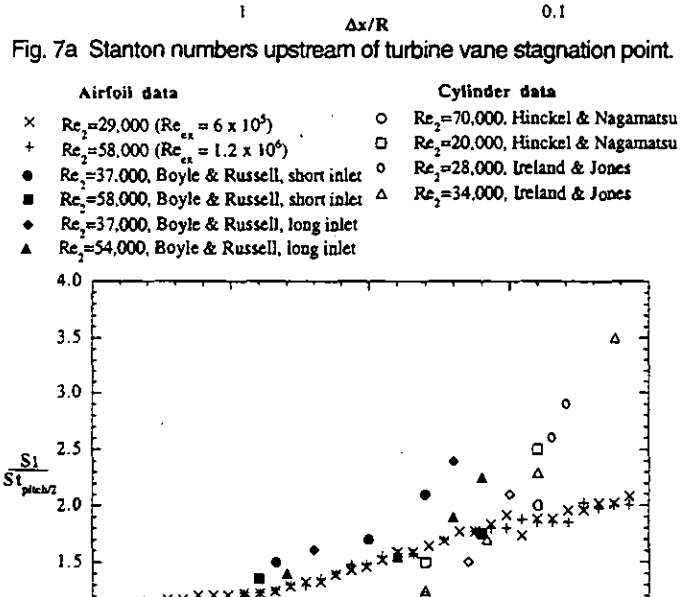

Fig. 7b Comparison of augmentation on the endwall at the stagnation line (St) normalized by midpitch value ($St_{pitch/2}$) with that given in the literature.

which is consistent with the heat transfer measurements. That is to say, there may be a corner vortex but, if so, it is very small. This also indicates that the existence of a large corner vortex seems to be geometry dependent.

Leading Edge Flowfield

As mentioned earlier, all three components of velocity were measured on the stagnation plane at the leading edge region of the stator vane. Figure 8a and 8b show the U-W vectors in this plane. Note that the streamwise distance has been normalized by the vane radius (R) while the spanwise has been normalized using the vane half-span (S). In each figure, the velocity vectors have been scaled by the respective inlet velocity. It is clear from these results that the density of the measurement locations is sufficient to document the leading edge vortex flowfield. For both Reynolds numbers, the inlet boundary layer separates as it approaches the stator vane and rolls up into a vortex motion which is accompanied by a downward movement of freestream fluid. The amount of this downward movement of fluid towards the endwall increases as the flow approaches the stator vane. As the gases away from the endwall are usually hotter in an actual turbine, this downwash would bring hot fluid in contact with the endwall and explains why the endwall-leading edge junction is a critical area from a design perspective.

Although the overall flow features are quite similar there are key differences between the two Reynolds number cases. At the high Reynolds number, the vortex is not as pronounced and does not extend as far into the span (z-direction) as compared with the low Reynolds number. For the low Reynolds number case the vectors indicate a more complete roll up of the leading edge vortex. This may be the consequence of the larger momentum that the flow carries at the high Reynolds number that the vortex motion is unable to overcome. Another difference is the location of the separation point which is closer to the stator vane for the low Reynolds number case. This can be seen in more detail by focusing on

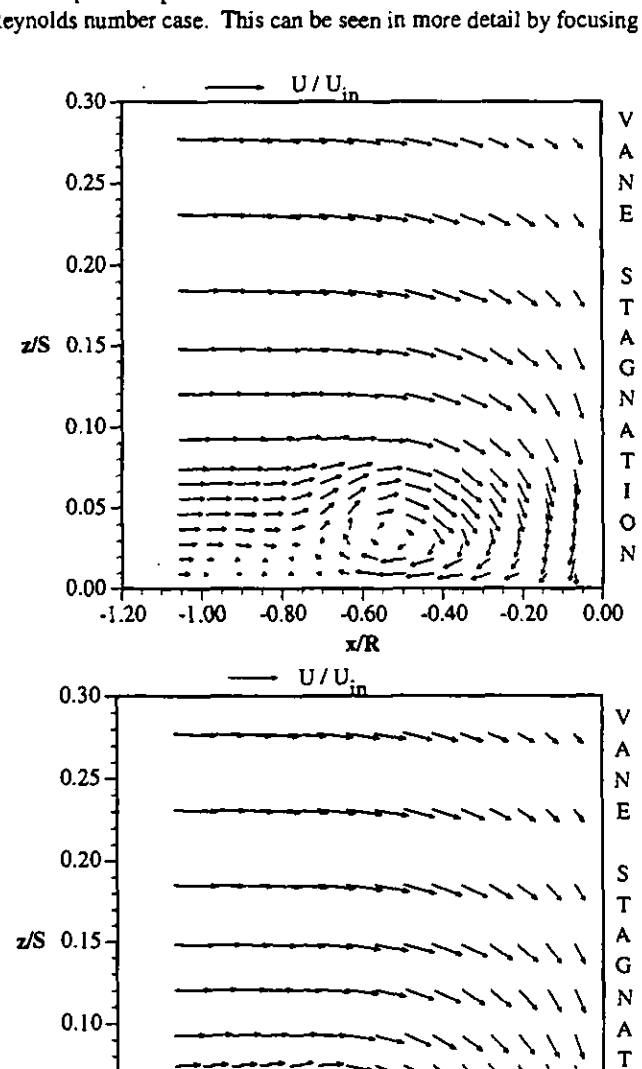

Fig. 8a,b Mean velocity vectors on the stagnation plane for Re_{ex} = 6x10⁵ (top) and 1.2x10⁶ (bottom).

Downloaded from http://asmedigitalcollection.asme.org/GT/proceedings-pdf/GT1998/78651/V004T09A035/2411331/v004t09a035-98-gt-173.pdf by guest on 20 August 2022

the streamwise velocity profiles as shown in Figures 9a and 9b. In order to see the separation better only the region near the wall ($z/S < 0.15$) has been plotted. Note that zero velocity lines associated with each profile are indicated as dashed vertical lines in these figures. Away from the wall, the velocity profiles flatten out as they approach the stator vane. Near the wall, the reverse flow becomes stronger going away from the stator vane and then decreases till the separation point is reached. This happens at about $x/R = -0.82$ at low Reynolds number and at $x/R = -0.99$ for the high Reynolds number. These profiles also identify the strong velocity gradients that mainly exist near the core of the leading edge vortex. The lower Reynolds number case shows larger velocity gradients especially near the core of the vortex. The velocity gradients are much smaller near the stator vane and upstream of the separation point. These gradients dictate the amount of turbulent kinetic energy in the flowfield and is discussed below.

Velocity fluctuations for all three components were combined to calculate the turbulent kinetic energy for the two Reynolds number cases. These results normalized by the inlet velocity are shown in Figures 10a and 10b. Both contours show maximum values centered about the core of the leading edge vortex. As the vortex core was formed closer to the stator vane for the low Reynolds number case, the peak k values are also closer to the stator vane as compared to the high Reynolds number case. In the streamwise direction, the turbulent kinetic energy levels decrease as one goes closer to the stator vane or further upstream. This is consistent with the location of the high velocity gradients as discussed above. The peak value of k is higher for the lower Reynolds number case because of a more complete roll up and the presence of stronger velocity gradients.

Figures 11a-c and 12a-c give contours of the rms levels of each of the fluctuating velocity components for the low and high Reynolds number cases normalized by the inlet velocity. In general, the peak values for all of the fluctuations occur at the same location which is at the center of the vortex core. For both the low and high Reynolds number cases, the u_{rms}/U_{in} and v_{rms}/U_{in} have similar contour patterns and have nominally the same levels. However, the vertical fluctuations, w_{rms}/U_{in}, are noticeably larger for the low Reynolds number as compared with the high Reynolds number. In addition, at the low Reynolds number the contours are asymmetrically skewed with higher gradients closer to the turbine vane. These higher levels can be attributed to the fact that for the low Reynolds number there is a complete turning of the vortex whereby there is a stronger vertical motion. The large gradients in the w_{rms}/U_{in} contours occur at the upstream edge of the vortex.

Another measure of the strength of the leading edge vortex can be obtained from the vorticity magnitude. By using a three-point second-order accurate differencing scheme for unequally spaced data the vorticity component normal to the stagnation plane, ω_y, was calculated. The results normalized using the vane chord and inlet velocity are shown in Figures 13a and 13b. The peak values for the vorticity magnitude is the same at both Reynolds numbers but for the vortex at low Reynolds number it is spread over a bigger region. This indicates a slightly stronger vortex motion at the low Reynolds number and is consistent with the results discussed earlier.

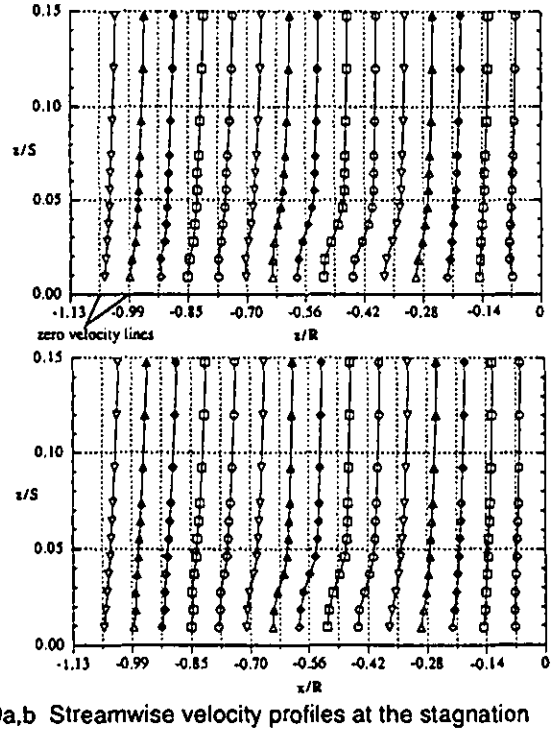

Fig. 9a,b Streamwise velocity profiles at the stagnation plane for $Re_{in} = 6x10^5$ (top) and $1.2x10^6$ (bottom).

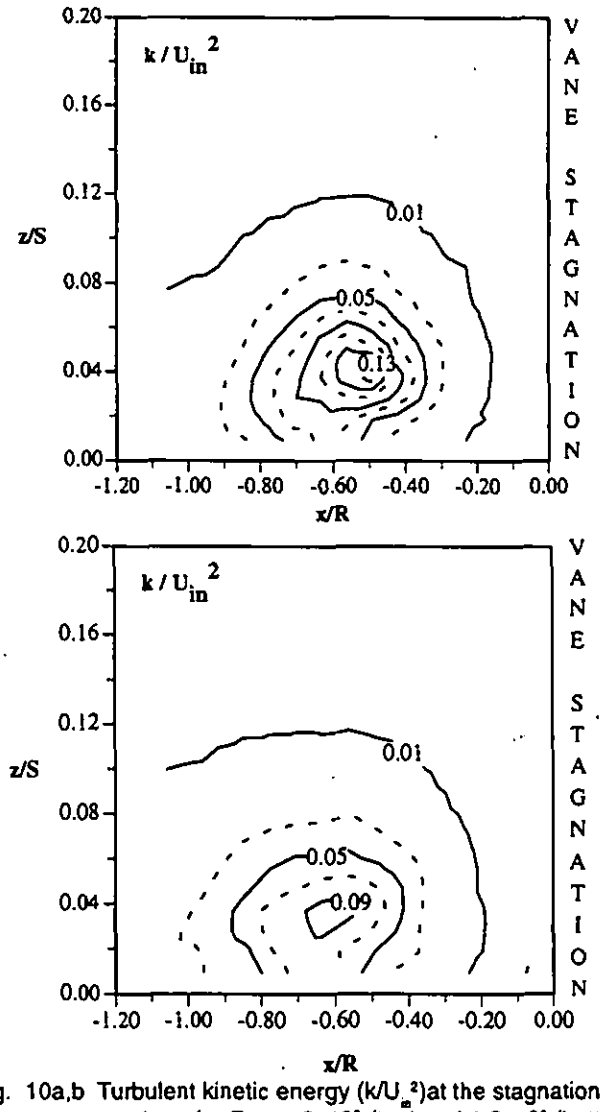

Fig. 10a,b Turbulent kinetic energy (k/U_{in}^2) at the stagnation plane for $Re_{in} = 6x10^5$ (top) and $1.2x10^6$ (bottom).

Downloaded from http://asmedigitalcollection.asme.org/GT/proceedings-pdf/GT1998/78651/V004T09A035/2411331/v004t09a035-98-gt-173.pdf by guest on 20 August 2022

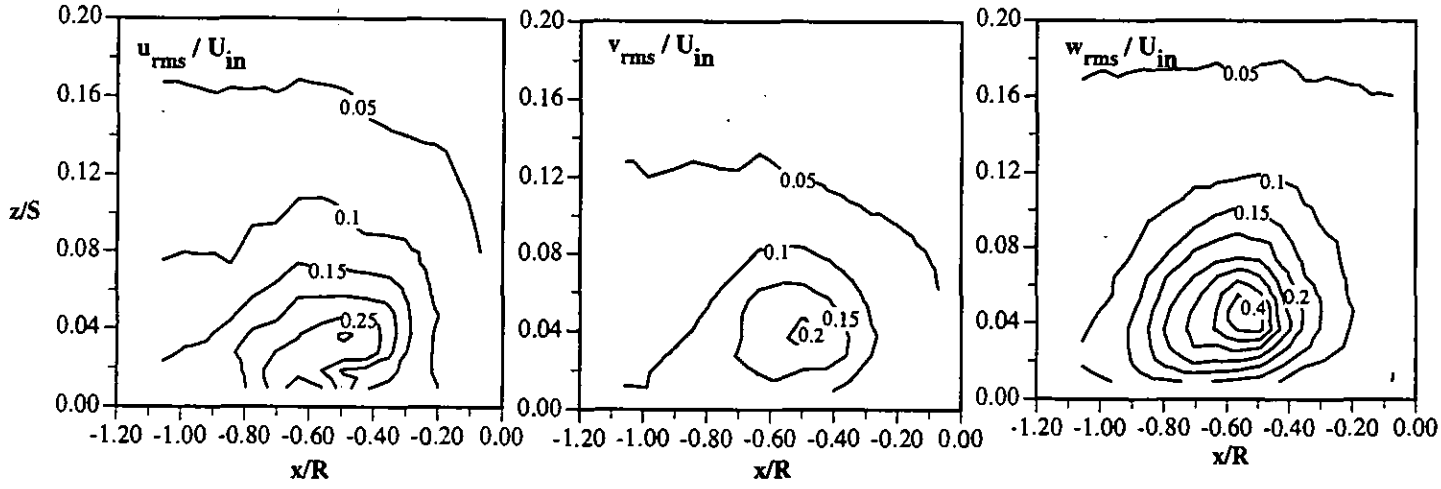

Fig. 11a,b,c. Normalized fluctuating velocities at the stagnation plane for $Re_{ex} = 6x10^5$.

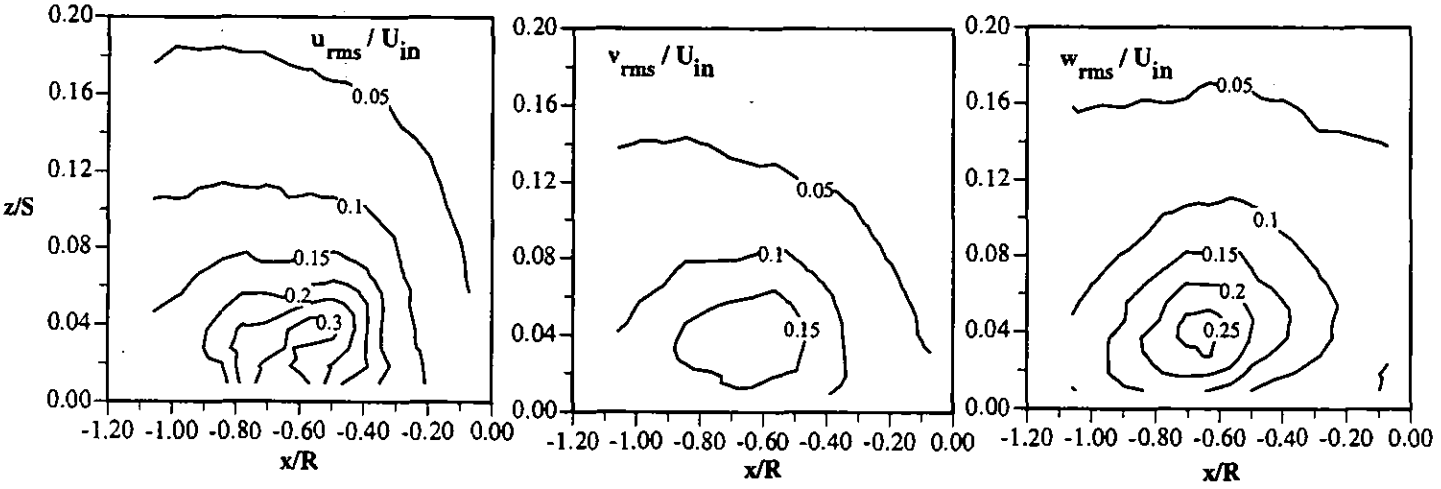

Fig. 12a,b,c. Normalized fluctuating velocities at the stagnation plane for $Re_{ex} = 1.2x10^6$.

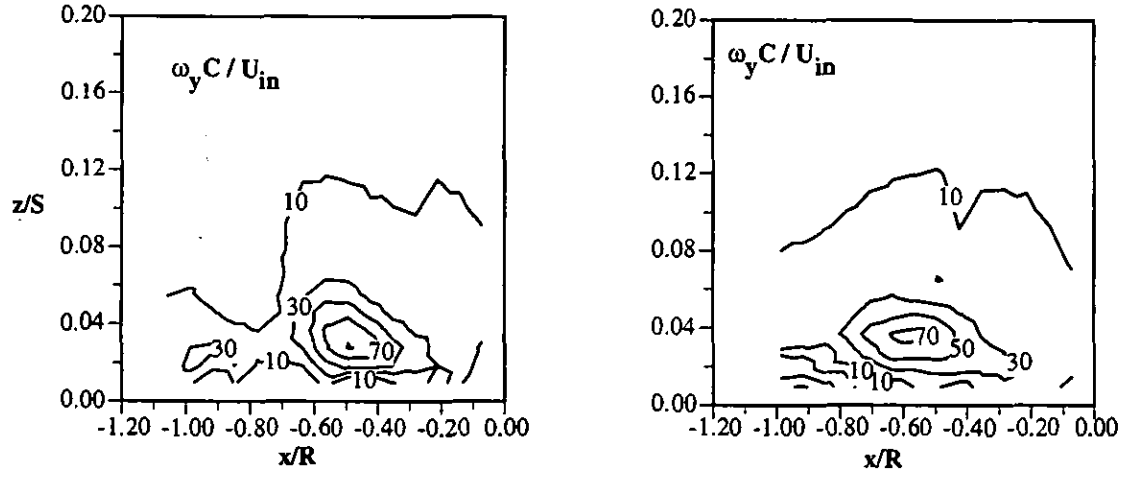

Fig. 13a,b. Normalized vorticity on the stagnation plane for $Re_{ex} = 6x10^5$ (left) and $1.2x10^6$ (right).

Downloaded from http://asmedigitalcollection.asme.org/GT/proceedings-pdf/GT1998/78651/V004T09A035/2411331/v004t09a035-98-gt-173.pdf by guest on 20 August 2022

Conclusions

This study has focused on determining the effects of Reynolds numbers on the static pressure and surface heat transfer distributions as well as the leading edge vortex for a modern, scaled-up turbine vane geometry. The test facility included a central airfoil with two leading edges representing the adjacent airfoils such that the passage vortex would be correctly simulated. All of the data, including endwall oil streakline visualizations, indicated that for the higher Reynolds number the passage vortex lifted off of the endwall onto the turbine vane thereby decreasing the endwall static pressure and causing a different surface heat transfer pattern. The heat transfer pattern was such that the peak Stanton number occurred at the suction surface for the high Reynolds number case as opposed to occurring more towards the center of the passage for the low Reynolds number case. The increase in the average Stanton numbers for the two Reynolds numbers could not be predicted using a flat plate turbulent boundary layer correlation. The peak heat transfer augmentation that occurred on the endwall nearest the stagnation position of the leading edge was a maximum of two times the heat transfer that occurred in the mid-span of the passage.

In the leading edge region, there were some clear differences in the flowfield characteristics of the leading edge vortices for the two different Reynolds numbers. While the separation of the boundary layer occurred slightly further upstream of the stagnation position for the higher Reynolds number, the vortex itself did not have a complete rotation for the higher Reynolds number. The lack of a complete rotation was attributed to the fact that at the higher Reynolds number there were too many inertial effects to overcome such that the upturn was not evident. Higher turbulent kinetic energy levels and a larger vorticity region were all consistent with the fact that the lower Reynolds number case had a stronger upturning vortex than the higher Reynolds number case.

Acknowledgments

The authors would like to thank Pratt & Whitney, W. Palm, Florida for their support of this work. In particular, thanks go to William Kvasnak and Fred Soechting for being the contract monitors.

References

Bailey, D. A. (1980) "Study of Mean- and Turbulent- Velocity Fields in a Large-Scale Turbine-Vane Passage," *ASME J of Engineering for Power*, Vol. 102, pp. 88 - 95.

Bangert, B. A., Kohli, A., Sauer, J. H. and Thole, K. A. (1997) "High Freestream Turbulence Simulation in a Scaled-up Turbine Vane Passage," ASME Paper No. 97-GT-51.

Boyle, R. J. and Russell, L. M. (1990) "Experimental Determination of Stator Endwall Heat Transfer," *ASME J of Turbomachinery*, Vol. 112, pp. 547 - 558.

Crawford, M.E.(1986) "Simulation Codes for Calculation of Heat Transfer to Convectively-Cooled Turbine Blades," 130 pp., a set of 4 lectures in Convective Heat Transfer and Film Cooling in Turbomachinery, T. Arts, ed., Lecture Series 1986-06, von Karman Institute for Fluid Dynamics, Rhode-Saint-Genese, Belgium.

Gaugler, R. E. and Russell, L. M. (1984) "Comparison of Visualized Turbine Endwall Secondary Flows and Measured Heat Transfer Patterns," *ASME J of Engineering for Gas Turbine and Power*, Vol. 106, pp.168-172.

Goldstein, R. J. and Spores, R. A. (1988) "Turbulent Transport on the Endwall in the Region Between Adjacent Turbine Blades," *ASME J of Heat Transfer*, Vol. 110, pp. 862-869.

Graziani, R. A., Blair, M. F., Taylor, J. R. and Mayle, R. E. (1980) "An Experimental Study of Endwall and Airfoil Surface Heat Transfer in a Large Scale Turbine Blade Cascade," *ASME J of Engineering for Power*, Vol. 102, pp. 257-267.

Hinckel, J. N. and Nagamatsu, H. T. (1986) "Heat Transfer in the Stagnation Region of the Junction of a Circular Cylinder Perpendicular to a Flat Plate," *International J Heat and Mass Transfer*, Vol. 29, pp. 999-1005.

Ireland, P. T. and Jones, T. V. (1986) "Detailed Measurements of Heat Transfer On and Around a Pedestal in Fully Developed Passage Flow," Proceedings of the 8th International Heat Transfer Conference, San Francisco, Vol. 3, Hemisphere Publishing Corporation, pp. 975-980.

Langston, L. S., Nice, M. L. and Hooper, R. M. (1977) "Three-Dimensional Flow Within a Turbine Cascade Passage," *ASME J of Engineering for Power*, Vol. 99, pp 21-28.

Marchal, P., and Sieverding, C. H. (1977) "Secondary Flows within Turbomachinery Bladings," *Secondary Flows in Turbomachines*, AGARD CP 214.

Mattingly, G. E. (1996) "Volume Flow Measurements," Fluid Mechanics Measurements, 2nd edition, edited by R. J. Goldstein (Taylor and Francis: New York).

Pierce, F. J. and Harsh, M. D. (1988) "The Mean Flow Structure Around and Within a Turbulent Junction or Horseshoe Vortex - Part II. The Separated and Junction Vortex Flow," *ASME J of Fluids Engineering*, Vol. 110, pp. 415-423.

Sieverding C. H. (1985) "Recent Progress in the Understanding of Basic Aspects of Secondary Flows in Turbine Blade Passages," *ASME J of Engineering for Gas Turbines and Power*, Vol. 107, pp. 248-257.

York, R. E., Hylton, L. D. and Mihelc, M. S. (1984) "An Experimental Investigation of Endwall Heat Transfer and Aerodynamics in a Linear Vane Cascade," ASME Paper No. 83-GT-51.

Downloaded from http://asmedigitalcollection.asme.org/GT/proceedings-pdf/GT1998/78651/V004T09A035/2411331/v004t09a035-98-gt-173.pdf by guest on 20 August 2022